Quasiperiodic Moiré Reconstruction and Modulation of Electronic Properties in Twisted Bilayer Graphene Aligned with Hexagonal Boron Nitride

Si-yu Li,[1,2] Zhiyue Xu,[3] Yingbo Wang,[2] Yingzhuo Han,[2] Kenji Watanabe,[5] Takashi Taniguchi,[6] Aisheng Song,[3,*] Tian-Bao Ma,[3] Hong-Jun Gao,[1,2,†] Yuhang Jiang,[4,‡] and Jinhai Mao[2,§]

[1]*Institute of Physics, Chinese Academy of Sciences, Beijing 100190, China*
[2]*School of Physical Sciences, University of Chinese Academy of Sciences, Beijing 100049, China*
[3]*State Key Laboratory of Tribology in Advanced Equipment, Tsinghua University, Beijing 100084, China*
[4]*College of Materials Science and Optoelectronic Technology, Center of Materials Science and Optoelectronics Engineering, University of Chinese Academy of Sciences, Beijing 100049, China*
[5]*Research Center for Electronic and Optical Materials, National Institute for Materials Science, 1-1 Namiki, Tsukuba 305-0044, Japan*
[6]*Research Center for Materials Nanoarchitectonics, National Institute for Materials Science, 1-1 Namiki, Tsukuba 305-0044, Japan*

(Received 31 May 2024; accepted 10 September 2024; published 6 November 2024)

Twisted van der Waals systems have emerged as intriguing arenas for exploring exotic strongly correlated and topological physics, with structural reconstruction and strain playing essential roles in determining their electronic properties. In twisted bilayer graphene aligned with hexagonal boron nitride (TBG/*h*-BN), the interplay between the two sets of moiré patterns from graphene-graphene (*G*-*G*) and graphene–*h*-BN ($G-h$-BN) interfaces can trigger notable moiré pattern reconstruction (MPR). Here, we present the quasiperiodic MPR in the TBG/*h*-BN with two similar moiré wavelengths, wherein the MPR results from the incommensurate mismatch between the wavelengths of the *G*-*G* and $G-h$-BN moiré patterns. The short-range, nearly ordered moiré super-superstructures deviate from moiré quasicrystal and are accompanied by inhomogeneous strain, thereby inducing spatially variable energy separations between the Van Hove singularities (VHs) in the band structures of the TBG near the magic angle. By tuning the carrier densities in our sample, correlated gaps at specific *AA* sites are observed, uncovering the quantum-dot-like behavior and incoherent characteristics of the *AA* sites in the TBG. Our findings would give new hints on the microscopic mechanisms underlying the abundant novel quantum phases in the TBG/*h*-BN.

DOI: 10.1103/PhysRevLett.133.196401

Moiré heterostructures composed of twisted two-dimensional (2D) materials hold significant potential for realizing novel quantum states, such as unconventional superconductivity, correlated insulators, and (fractional) Chern insulators [1–7]. When three or more layers are stacked, moiré patterns can interfere with each other, giving rise to new super-superstructures and profoundly modulating the topography and electronic properties of the heterostructures [4,8–12]. One celebrated example is twisted multilayer graphene, wherein "moiré of moiré" and more robust superconductivity than that in magic-angle twisted bilayer graphene (MATBG) have been observed [4,13–16].

Besides graphene-graphene (*G*-*G*) interface, moiré patterns can originate from graphene-hexagonal boron nitride ($G-h$-BN) interface [17–20]. In twisted bilayer graphene aligned with *h*-BN (TBG/*h*-BN), (quantized) anomalous Hall effect, charge density wave (CDW) and fractional Chern insulators have been reported [5,21–23]. The two sets of moiré patterns in the TBG/*h*-BN have strong coupling and significant structural reconstruction when their wavelengths are similar. Nevertheless, in-depth microscale investigations on the moiré pattern reconstruction (MPR) and its exact impacts on the band structures remain insufficient, which are vital for understanding the novel quantum states in the TBG/*h*-BN and will contribute to establishing a valuable platform for exploring strongly correlated and topological physics.

In this Letter, we employ a 4.8-K ultrahigh-vacuum ($\sim 10^{-11}$ mbar) scanning tunneling microscopy (STM) to directly visualize the two sets of moiré patterns. The fast Fourier transform (FFT) analysis of the large-scale topography shows the two sets of moiré reciprocal lattices. Through inverse FFT, we categorize the origins of these moiré reciprocal lattices based on the distinct topographic structures of the *G*-*G* and $G-h$-BN moiré patterns. In our proposed rigid model, the mismatch between the two moiré wavelengths would generate a new moiré

*Contact author: songas@mail.tsinghua.edu.cn
†Contact author: hjgao@iphy.ac.cn
‡Contact author: yuhangjiang@ucas.ac.cn
§Contact author: jhmao@ucas.ac.cn

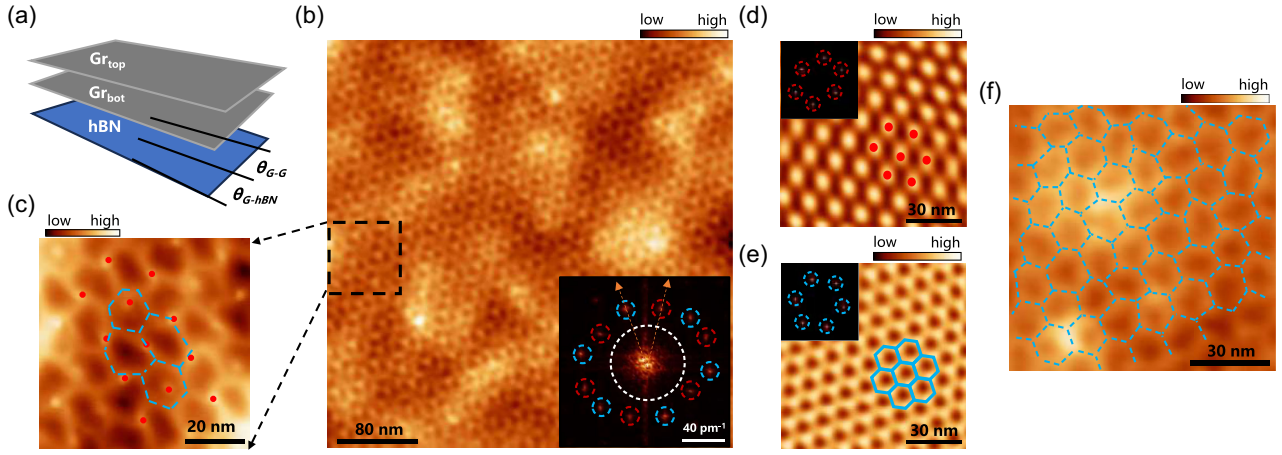

FIG. 1. (a) The schematic view of the TBG/h-BN moiré heterostructure. (b) The large-scale STM topography of the TBG/h-BN device ($V_b = -1$ V, $I = 60$ pA). The inset is its FFT result. The G-G ($G-h$-BN) moiré Bragg peaks are marked by the red (blue) circles. The white circle highlights the blurry signals from background undulations. (c) The close-up topography of (b) that shows the two sets of moiré patterns, where the G-G ($G-h$-BN) moiré patterns are marked by the red spots (blue hexagons). (d),(e) The one-fourth of the inverse FFT images from the Bragg peaks presented in the insets. (f) The distorted $G-h$-BN moiré patterns obtained by deducting the G-G moiré patterns shown in (d) from the topography shown in (b).

super-superstructure, which can be referred as moiré quasicrystal [24]. However, short-range quasiperiodic super-superstructures with prominent MPR are formed. Our simulation results closely replicate the STM topography. Interestingly, scanning tunneling spectroscopy (STS) spectra obtained at different AA sites of the TBG exhibit notable differences, manifested as the variations of the energy separation between the two Van Hove singularities (VHs). By tuning the carrier density, we find the existences of correlated gaps at certain AA sites. These anomalies indicate that the local electronic structures are significantly modulated by the MPR, and the incoherence between the AA sites. Our findings reveal the microscopic behaviors of the MPR in the TBG/h-BN wherein the G-G and $G-h$-BN moiré are similar in wavelengths, and would help the future research on the microscopic origins of the novel transport phenomena, such as CDW at fractional filling and the spatial evolution of orbital ferromagnetism [5,21,22,25,26].

The schematic view of our TBG/h-BN sample [27,28] (details in Supplemental Material, Sec. S1 [29]) is shown in Fig. 1(a). The bottom graphene (Gr_{bot}) is rotated by θ_{bot} with respect to the h-BN substrate, and the top graphene (Gr_{top}) is rotated by θ_{TBG} with respect to the Gr_{bot}. The large-scale topography is presented in Fig. 1(b). The inset is its FFT, where two groups of Bragg peaks are identified by the red and the blue circles. Figure 1(c) displays the close-up topographic image, which vividly illustrates the existence of two sets of moiré patterns with similar wavelengths (~15 nm), marked by the red spots and the blue hexagons, respectively. Considering the distinct configurations of the G-G and $G-h$-BN moiré patterns, we extract these Bragg peaks separately and perform inverse FFT. The inverse FFT results are presented in Figs. 1(d) and 1(e). In Fig. 1(d), triangular lattices marked by the red dots obviously originate from the TBG [30,31] (wavelength $L_{G\text{-}G} \approx 15.0$ nm, twist angle $\theta_{G\text{-}G} \approx 0.94°$, Supplemental Material, Sec. S2 [29]). Hexagonal structures highlighted by the blue hexagons in Fig. 1(e) suggest these moiré patterns result from twisted $G-h$-BN interface [17,19] (wavelength $L_{G-h\text{-BN}} \approx 14.4$ nm, twist angle $\theta_{G-h\text{-BN}} \approx 0°$, Supplemental Material, Sec. S2 [29]). From the intersection angle between the two groups of Bragg peaks, we conclude that the orientation angle between the two sets of moiré patterns is approximately 30°. Our TBG/h-BN sample is quite different from those in the previous works, for the wavelengths of the G-G and $G-h$-BN moiré patterns are highly similar and close to the MATBG [32,33]. One noteworthy feature in Fig. 1(c) is that the $G-h$-BN moiré deform into irregular hexagons, which is absent in Fig. 1(e). This inconsistency comes from the fact that the inverse FFT result solely from the Bragg peaks in the blue circles loses fine information about the structure deformation. To solve this drawback, we extract the G-G moiré, obtained by inverse FFT, from the raw topography. The result is displayed in Fig. 1(f), where the deformation of the $G-h$-BN moiré is illustrated (Supplemental Material, Sec. S2 [29]).

The remarkable structural deformation in Figs. 1(c) and 1(f) indicates that the coupling between the two sets of moiré patterns is strong. In order to clarify the coupling effects between them, we first produce a topographic structure with the wavelengths measured from Figs. 1(d) and 1(e), in the absence of structural relaxation (Supplemental Material, Sec. S3 [29]) [32]. The simulated image in Fig. 2(a) shows moiré super-superstructures with a wavelength ~75 nm, marked by the white rhombus and the

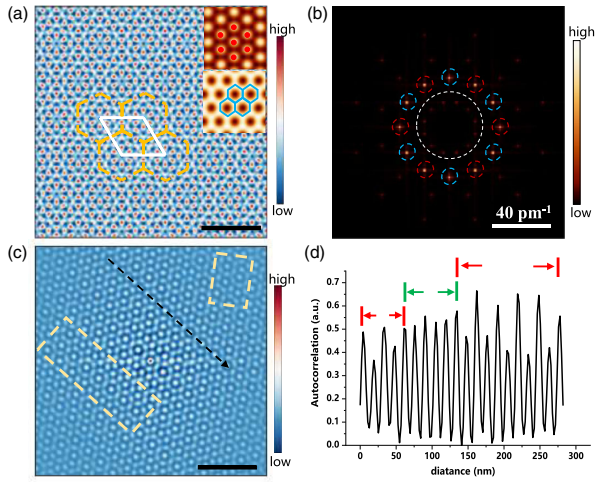

FIG. 2. (a) The simulated topography illustrating the moiré super-superlattices, marked by the yellow hexagons and the white rhombus. The moiré wavelengths used for simulation are measured from Figs. 1(d) and 1(e). The insets are the G-G ($G-h$-BN) moiré patterns from the Bragg peaks shown in (b). (b) The FFT of (c). Bragg peaks from the G-G ($G-h$-BN) moiré patterns are marked by the red (blue) circles. The white circle highlights the Bragg peaks from the moiré super-superlattices. (c) The autocorrelation map of the topography shown in Fig. 1(b), obtained by deducting background undulations. (d) The line profile along the black arrow in (c), showing a transition of the periodicity of λ to 2λ ($\lambda \sim 15$ nm). Scale bars, 100 nm.

yellow hexagons. The insets are the G-G and $G-h$-BN moiré patterns from Fig. 2(b), the FFT of Fig. 2(a), where the red (blue) circles highlight the Bragg peaks from the G-G ($G-h$-BN) moiré patterns. The Bragg peaks marked by the white circles in Fig. 2(b) come from the newly formed super-superstructures. Compared with the simulated results, the dispersive Bragg signals surrounded by the white circle in Fig. 1(b) indicate that no long-range ordered super-superstructures exists. The difference between the simulated and real FFT reveals that structural relaxation strongly shapes the topographic structures and results in remarkable MPR, especially when the periods of the moiré patterns are similar [11,34]. To study the structure evolution and the details of the MPR, we calculate the autocorrelation map of the STM topography shown in Fig. 1(b), after deducting the background undulations (Supplemental Material, Sec. S4 [29]). The autocorrelation map shown in Fig. 2(c) depicts that no globally ordered super-superstructures but short-range nearly ordered super-superstructures with a double wavelength than the G-G ($G-h$-BN) moiré patterns are formed, highlighted by the golden rectangles. This is further confirmed by the line profile [Fig. 2(d)] along the black arrow in Fig. 2(c), in which a transition from the periodicity of λ to 2λ happens ($\lambda \sim 15$ nm) (Supplemental Material, Sec. S4 [29]).

Inspired by the emergent short-range super-superstructures with 2λ wavelength, we propose a rigidly incommensurate

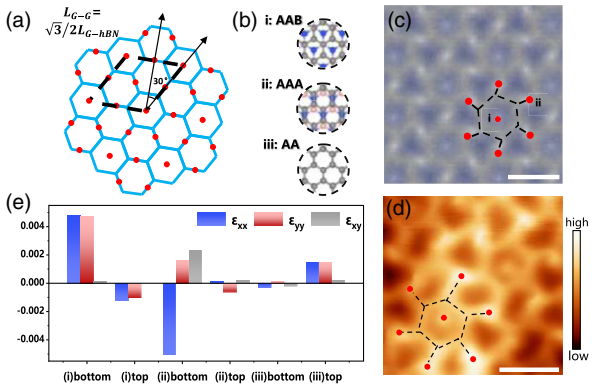

FIG. 3. (a) The rigid model of the incommensurate overlapping between the two sets of moiré patterns. The blue hexagons (red dots) represent the $G-h$-BN (the AA sites of the G-G) moiré patterns. The black parallelogram represents the supersuperlattice with a wavelength of $2L_{G-G}$. (b) The atomic configurations of the AAA/AAB sites in TBG/h-BN and the AA sites in TBG (gray, C atoms; blue, N atoms; pink, B atoms). (c) The simulated result of the incommensurate model shown in (a) by molecular dynamics. The super-superstructure is marked by black lines and the red dots. The AAA (AAB) sites are marked by i (ii). (d) The STM topographic image, hosting similar structures with (c). (e) the calculated local strain ε at the high-symmetry sites denoted as AAA/AAB in TBG/h-BN and AA in TBG. Scale bars, 20 nm.

model to describe how the two sets of moiré patterns overlap with each other, as shown in Fig. 3(a), wherein the wavelengths of the moiré patterns should meet the criterions: $L_{G\text{-}G} = \sqrt{3}/2L_{G-h\text{-BN}}$ and the orientation angle between them is 30°. A new super-superlattice marked by a black parallelogram in Fig. 3(a) is formed, hosting a wavelength of $2L_{G\text{-}G}$. For $\theta_{G-h\text{-BN}} \approx 0°$, this incommensurate criterion requires $\theta_{G\text{-}G} \approx 1.1°$, which is very close to the magic angle (~1.05°). Considering the significant impact of structural relaxation, we employ molecular dynamics (MD), which allows atoms to relax to the force equilibrium position (Supplemental Material, Sec. S5 [29]), so providing a more realistic depiction of the topographic structure than the rigid model. Figure 3(c) illustrates the corresponding computational results, which hosts "helical-flower-like" super-superstructures with a period of $2L_{G\text{-}G}$, consisting of one AAB site (i) and six helically arranged AAA sites (ii). These super-superstructures resemble the short-range super-superstructures in the small-scale STM image in Fig. 3(c), which are highlighted by the red spots and the black lines. With the similarity between the simulation and the STM topography, we conclude that the MPR still tends to realize short-range ordered super-superstructures but not moiré quasicrystal, when the length scales of the two sets of moiré patterns are close but incommensurate in the TBG/h-BN. Such a tendency may be a universe in the systems with multiple sets of moiré patterns, and would produce domains consisting of superstructures with different length scales under certain conditions [11,14,34–36].

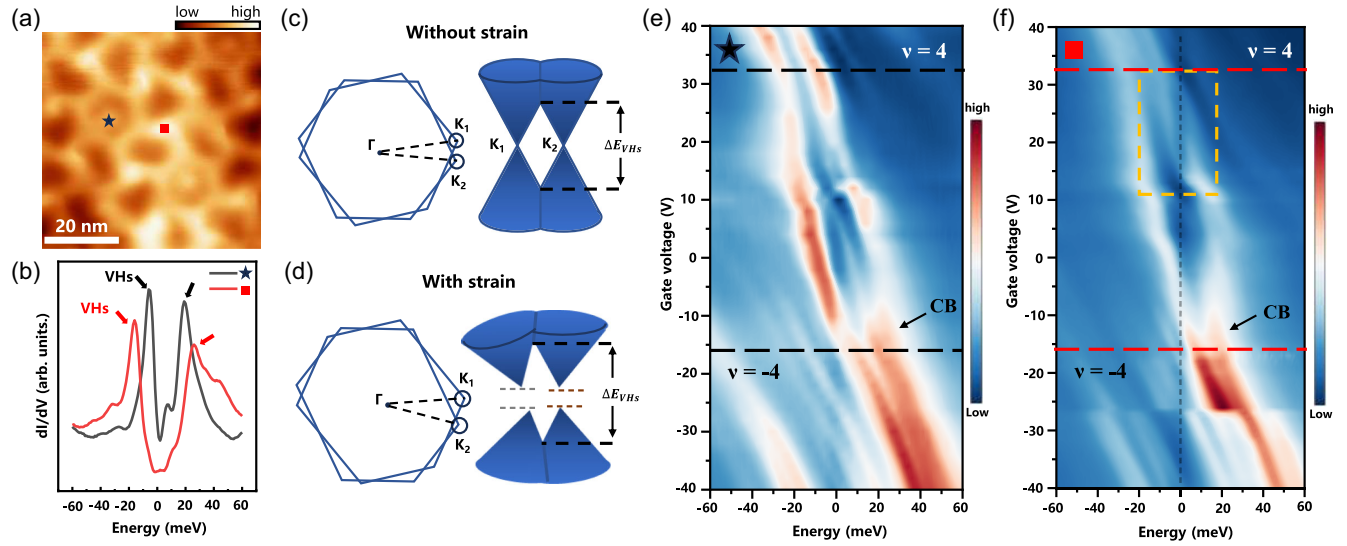

FIG. 4. (a) The small-scale STM topographic image. (b) The dI/dV spectra measured at the two AA sites at gate voltage $V_g = 0$ V ($V_b = -60$ mV and $I = 100$ pA). The arrows highlight the intense peaks originating from the VHs. (c),(d) Illustration of the emergence of VHs in the TBG as a consequence of the rotation in reciprocal space. (c) without strain, (d) with strain. Γ, K_1 and K_2 denote points in the Brillouin zone of the single layer graphene. ΔE_{VHs} denotes the energy separations between the VHs. (e),(f) The color contours of the dI/dV evolution as a function of back gate voltage (V_g) at the AA sites marked in (e) and (f). The yellow rectangle in (f) highlights the correlated gap. The horizontal lines mark the empty (full) filling voltages (the filling factor $\nu = -4$ or 4). The vertical line: the Fermi level. CB: the conduction bands.

Albeit at the cost of elastic energy, the MPR occurs owing to the differences in configuration energy among distinct stacking regions of moiré patterns [11,37–40]. One notable feature in Figs. 3(c) and 3(d) is that the hexagonal $G-h$-BN moiré patterns deform into irregular shapes. We attribute the observed MPR to the overlapping and coupling between the AA sites of the G-G moiré patterns and the AA (BA) sites of the $G-h$-BN moiré patterns. These sites host high configuration energy, and the system tends to minimize the overlapping area between them to achieve a lower total energy [37,41,42]. Therefore, the atoms at these sites are inclined to relax into a lower energy configuration, thus induces the deformation of the $G-h$-BN moiré patterns.

The MPR in our sample is expected to generate unignorable strain. Numerous theoretical and experimental works have conclusively demonstrated that strain can profoundly influence the band structures of moiré heterostructures [43–45]. In Fig. 3(e), we present the calculated local strain at high-symmetry sites denoted as AAA/AAB in the TBG/h-BN and AA in the pristine TBG, based on their atomic configurations, as shown in Fig. 3(b). Because of the MPR, strain at high-symmetry sites in the TBG/h-BN is much larger than in the pristine TBG. For directly interfacing with the h-BN substrate, $\mathrm{Gr}_{\mathrm{bot}}$ experiences stronger strain compared to $\mathrm{Gr}_{\mathrm{top}}$. Another noteworthy point is that the local shear strain in the AAA sites is much larger than in the AAB sites, in agreement with the topographic characters of the super-superstructures marked in Fig. 3(c), wherein the AAA sites exhibit more pronounced shear distortion compared to the AAB sites.

To investigate the impacts of the MPR on the band structures of the heterostructure, we initially focus on the two AA sites marked in Fig. 4(a). Figure 4(b) shows the two measured dI/dV spectra, which are gained by standard lock-in technique, with 2 mV ac modulation added on the dc sample bias. The spectra feature two intense peaks originating from the VHs in the band structures of the TBG. Interestingly, the energy separations between the VHs (ΔE_{VHs}) at the two AA sites differ from each other significantly ($\Delta E_{\mathrm{VHs}} \approx 41$ meV, the red square; $\Delta E_{\mathrm{VHs}} \approx 25$ meV, the black pentagram). We further measure ΔE_{VHs} at other AA sites in Fig. 4(a), and find that they vary without a specific regularity (Supplemental Material, Sec. S6 [29]). In the pristine TBG, the ΔE_{VHs} at different AA sites should be identical [46]. Figure 4(c) illustrates the emergence of VHs as a consequence of the rotation of two undistorted monolayer-graphene Dirac cones rotated about the Γ point in the Brillouin zone. With different ΔE_{VHs}, we conclude that the local structural and electronic properties at these AA sites are unalike with each other.

Under strain, the Dirac cones of graphene deform with changed Fermi velocities V_F and changed wave vectors of the Dirac points [47–49], shown in Fig. 4(d). Furthermore, the C_{2Z} symmetry of graphene is broken by the staggered sublattice potential and the Dirac points are gapped when aligned with h-BN. The local gaps may vary spatially owing to the structural reconstruction of the $G-h$-BN

moiré patterns [20,42]. Taking the above factors into consideration, we propose that the random spatial modulation of ΔE_{VHs} is attributed to the uneven strain stemming from the irregular MPR. The spatially dependent positions of the Dirac points, the V_F and gaps would naturally lead to the spatial variation of ΔE_{VHs} (Supplemental Material, Sec. S6 [29]). The prominent differences between ΔE_{VHs} reveal the important roles of the MPR on defining the local electronic properties and the actual twist angle of the TBG. Our observation about the local inhomogeneity of the band structures offers a microscopic insight into the reported spatially dependent experimental phenomena in the moiré heterostructures [22,26]. Moreover, the inconsistencies between transport measurements of the TBG devices with almost the same twist angles may be due to the complex structural relaxation, as observed in our experiments.

In TBG/h-BN heterostructures, novel quantum states have been found, such as CDW and fractional Chern insulators [5]. The broken C_{2Z} symmetry gaps the Dirac points and conduce to the formation of topological flat bands, but the nature of the correlation-induced states is still not completely clear. To explore the electron correlation effects, we tune the electron filling of our sample by the back gate and trace the evolution of the dI/dV spectra. Figures 4(e) and 4(f) present the $dI/dV(V_b, V_g)$ spectra measured at the AA sites marked in Fig. 4(a), respectively, where the horizontal lines mark the empty (full) filling voltages (the filling factor $\nu = -4$ or 4). Both spectra host a series of peaks from remote bands which are absent in the pristine TBG. These replica peaks correspond to the VHs in replica remote bands, potentially resulting from Brillouin-zone folding [32]. When the conduction band (CB) at the AA site marked by the red square is doped to the Fermi level, it splits with a maximum gap of approximately 11.5 meV. This band splitting is believed to arise from the electron correlation, for it only appears at the partial doping [30,31]. On the contrary, the CB at the AA site marked by the black pentagram exists no band splitting during the whole process of doping (more results in Supplemental Material, Sec. S7 [29]). The astonishing difference between the evolution of the CB with doping at the AA sites indicates the MPR and strain can dramatically disturb the correlated states. More importantly, our experimental results provide the signature of correlation effects existing at one single AA site of the TBG, which suggests the AA sites are quantum-dot-like and the long-range Coulomb interaction may not play a decisive role. Considering the closeness of the twist angles, our observations about the spatially various ΔE_{VHs} and correlated gaps provide new insights into the related measurements about the topological and correlated states in the TBG/h-BN [5,6,21–23,25,50]. Furthermore, the incoherence between the AA sites sets a constraint on the theoretical models about the mechanisms of correlated states in the TBG, and would inspire the further understanding of the exotic physics in moiré heterostructures [51–53].

In summary, the coupling between the two sets of moiré patterns with similar wavelengths in our TBG/h-BN device is shown to incline toward forming short-range and nearly ordered moiré super-superstructures, which triggers remarkable MPR, thus provoking intense and nonuniform strain. These super-superstructures locally expand the unit moiré cell and may play a certain role in the formation of CDW. The energy separations between the VHs (ΔE_{VHs}) are shown to be irregularly variable between the different AA sites in the moiré patterns of the TBG, which can be attributed to the uneven strain from the MPR. The related results manifest the strong influence of the MPR on the band structures of the TBG. Moreover, the observation that the ΔE_{VHs} vary spatially and the correlated gaps still exist at a minority of the AA sites during doping the device unveils the incoherence between the AA sites in the TBG, which would be helpful for the further study of novel moiré physics.

Acknowledgments—We acknowledge financial support from the National Key R&D Program of China with Grant No. 2019YFA0307800 (J. M.), National Natural Science Foundation of China (NSFC) with Grants No. 11974347 (J. M.), No. 12474477 (J. M.), No. 12074377 (Y. J.), the National Natural Science Foundation of China (Grants No. 52225502, No. 52305200, No. 52363033), the China Postdoctoral Science Foundation (Certificate No. 2024M753465), the Postdoctoral Fellowship Program (Grade C) of China Postdoctoral Science Foundation (Grant No. GZC20241893), Fundamental Research Funds for the Central Universities (J. M. and Y. J.), the EMEXT Element Strategy Initiative to Form Core Research Center through Grant No. JPMXP0112101001 (K. W. and T. T.).

S.-y. L, Y. W., and Z. X. contributed equally to this work.

[1] Y. Cao *et al.*, Nature (London) **556**, 80 (2018).
[2] Y. Cao, V. Fatemi, S. Fang, K. Watanabe, T. Taniguchi, E. Kaxiras, and P. Jarillo-Herrero, Nature (London) **556**, 43 (2018).
[3] K. P. Nuckolls, M. Oh, D. Wong, B. Lian, K. Watanabe, T. Taniguchi, B. A. Bernevig, and A. Yazdani, Nature (London) **588**, 610 (2020).
[4] J. M. Park, Y. Cao, K. Watanabe, T. Taniguch, and P. Jarillo-Herrero, Nature (London) **590**, 249 (2021).
[5] Y. Xie *et al.*, Nature (London) **600**, 439 (2021).
[6] A. T. Pierce *et al.*, Nat. Phys. **17**, 1210 (2021).
[7] H. Polshyn *et al.*, Nature (London) **588**, 66 (2020).
[8] Z. Wang *et al.*, Sci. Adv. **5**, eaay8897 (2019).
[9] L. Wang, S. Zihlmann, M.-H. Liu, P. Makk, K. Watanabe, T. Taniguchi, A. Baumgartner, and C. Schönenberger, Nano Lett. **19**, 2371 (2019).
[10] X. Sun *et al.*, Nat. Commun. **12**, 7196 (2021).

[11] S. Turkel *et al.*, Science **376**, 193 (2022).
[12] W.-J. Zuo, J.-B. Qiao, D.-L. Ma, L.-J. Yin, G. Sun, J.-Y. Zhang, L.-Y. Guan, and L. He, Phys. Rev. B **97**, 035440 (2018).
[13] X. Liu, N. J. Zhang, K. Watanabe, T. Taniguchi, and J. I. A. Li, Nat. Phys. **18**, 522 (2022).
[14] H. Kim *et al.*, Nature (London) **606**, 494 (2022).
[15] J. M. Park, Y. Cao, L.-Q. Xia, S. Sun, K. Watanabe, T. Taniguchi, and P. Jarillo-Herrero, Nat. Mater. **21**, 877 (2022).
[16] Y. Cao, J. M. Park, K. Watanabe, T. Taniguchi, and P. Jarillo-Herrero, Nature (London) **595**, 526 (2021).
[17] M. Yankowitz, Q. Ma, P. Jarillo-Herrero, and B. J. LeRoy, Nat. Rev. Phys. **1**, 112 (2019).
[18] E. Wang *et al.*, Nat. Phys. **12**, 1111 (2016).
[19] J. Xue, J. Sanchez-Yamagishi, D. Bulmash, P. Jacquod, A. Deshpande, K. Watanabe, T. Taniguchi, P. Jarillo-Herrero, and B. J. LeRoy, Nat. Mater. **10**, 282 (2011).
[20] C. R. Woods *et al.*, Nat. Phys. **10**, 451 (2014).
[21] A. L. Sharpe, E. J. Fox, A. W. Barnard, J. Finney, K. Watanabe, T. Taniguchi, M. A. Kastner, and D. Goldhaber-Gordon, Science **365**, 605 (2019).
[22] M. Serlin, C. L. Tschirhart, H. Polshyn, Y. Zhang, J. Zhu, K. Watanabe, T. Taniguchi, L. Balents, and A. F. Young, Science **367**, 900 (2020).
[23] A. L. Sharpe, E. J. Fox, A. W. Barnard, J. Finney, K. Watanabe, T. Taniguchi, M. A. Kastner, and D. Goldhaber-Gordon, Nano Lett. **21**, 4299 (2021).
[24] A. Uri *et al.*, Nature (London) **620**, 762 (2023).
[25] C. L. Tschirhart *et al.*, Science **372**, 1323 (2021).
[26] S. Grover *et al.*, Nat. Phys. **18**, 885 (2022).
[27] S.-y. Li *et al.*, Nat. Commun. **13**, 4225 (2022).
[28] S. Li, Z. Wang, Y. Xue, L. Cao, K. Watanabe, T. Taniguchi, H. Gao, and J. Mao, Chin. Phys. B **32**, 067304 (2023).
[29] See Supplemental Material at http://link.aps.org/supplemental/10.1103/PhysRevLett.133.196401 for (1) methods of sample fabrication, (2) descriptions of molecular dynamics simulation, (3) details of data analysis and (4) additional results of samples different from that in the main text.
[30] Y. Xie, B. Lian, B. Jäck, X. Liu, C.-L. Chiu, K. Watanabe, T. Taniguchi, B. A. Bernevig, and A. Yazdani, Nature (London) **572**, 101 (2019).
[31] A. Kerelsky *et al.*, Nature (London) **572**, 95 (2019).
[32] D. Wong, K. P. Nuckolls, M. Oh, R. L. Lee, K. Watanabe, T. Taniguchi, and A. Yazdani, Low Temp. Phys. **49**, 655 (2023).
[33] X. Huang, L. Chen, S. Tang, C. Jiang, C. Chen, H. Wang, Z.-X. Shen, H. Wang, and Y.-T. Cui, Nano Lett. **21**, 4292 (2021).
[34] X. Lai, D. Guerci, G. Li, K. Watanabe, Takashi Taniguchi, J. Wilson, J. H. Pixley, and E. Y. Andrei, arXiv:2311.07819.
[35] I. M. Craig *et al.*, Nat. Mater. **23**, 323 (2024).
[36] M. Anđelković, S. P. Milovanović, L. Covaci, and F. M. Peeters, Nano Lett. **20**, 979 (2020).
[37] M. R. Rosenberger, H.-J. Chuang, M. Phillips, V. P. Oleshko, K. M. McCreary, S. V. Sivaram, C. S. Hellberg, and B. T. Jonker, ACS Nano **14**, 4550 (2020).
[38] I. Maity, P. K. Maiti, H. R. Krishnamurthy, and M. Jain, Phys. Rev. B **103**, L121102 (2021).
[39] N. P. Kazmierczak *et al.*, Nat. Mater. **20**, 956 (2021).
[40] M. M. v. Wijk, A. Schuring, M. I. Katsnelson, and A. Fasolino, 2D Mater. **2**, 034010 (2015).
[41] H. Yoo *et al.*, Nat. Mater. **18**, 448 (2019).
[42] P. San-Jose, A. Gutiérrez-Rubio, M. Sturla, and F. Guinea, Phys. Rev. B **90**, 075428 (2014).
[43] A. Sinner, P. A. Pantaleón, and F. Guinea, Phys. Rev. Lett. **131**, 166402 (2023).
[44] F. Mesple, A. Missaoui, T. Cea, L. Huder, F. Guinea, G. Trambly de Laissardière, C. Chapelier, and V. T. Renard, Phys. Rev. Lett. **127**, 126405 (2021).
[45] L. Huder, A. Artaud, T. Le Quang, G. T. de Laissardière, A. G. M. Jansen, G. Lapertot, C. Chapelier, and V. T. Renard, Phys. Rev. Lett. **120**, 156405 (2018).
[46] I. Brihuega, P. Mallet, H. González-Herrero, G. Trambly de Laissardière, M. M. Ugeda, L. Magaud, J. M. Gómez-Rodríguez, F. Ynduráin, and J. Y. Veuillen, Phys. Rev. Lett. **109**, 209905(E) (2012).
[47] F. de Juan, M. Sturla, and M. A. H. Vozmediano, Phys. Rev. Lett. **108**, 227205 (2012).
[48] S.-M. Choi, S.-H. Jhi, and Y.-W. Son, Phys. Rev. B **81**, 081407(R) (2010).
[49] W.-J. Jang *et al.*, Carbon **74**, 139 (2014).
[50] M. Chen, Y. Xie, B. Cheng, *et al.*, Nat. Nanotechnol. **19**, 962 (2024).
[51] Z.-D. Song and B. A. Bernevig, Phys. Rev. Lett. **129**, 047601 (2022).
[52] H. Hu *et al.*, Phys. Rev. Lett. **131**, 166501 (2023).
[53] Y. H. Kwan, G. Wagner, N. Chakraborty, S. H. Simon, and S. A. Parameswaran, Phys. Rev. B **104**, 115404 (2021).